Nanoscale

PAPER

View Article Online
View Journal

Cite this: DOI: 10.1039/d6nr00820h

Modified sol–gel synthesis greatly improves textural properties and photocatalytic performance of Cu-doped phase-pure $ZnAl_2O_4$

Syed Ansar Ali Shah, [a] Mudasar Nazir,[b] Steve Dunn,[b] Muhammad Tariq Sajjad *[b] and Richard T. Baker *[a]

This work addresses the dual challenges of sustainable H_2 production and wastewater treatment. We developed high-performance Cu-doped $ZnAl_2O_4$ (ZAO) spinels through a modified sol–gel citrate route. Calcination under N_2 with a limited O_2 supply harnesses residual citrate-derived carbon to confine crystal growth, yielding phase-pure nanocrystalline $Zn_{1-x}Cu_xAl_2O_4$ materials (x = 0.01–0.2) with uniform mesopores and a fourfold increase in surface area *versus* conventional sol–gel synthesis. Elemental mapping confirmed uniform Cu incorporation, while ICP-MS confirmed the target stoichiometry. XPS confirmed an increase in oxygen vacancy concentrations with increasing Cu doping, and bandgap engineering (3.95 to 2.33 eV) enabled broad visible-light absorption at the higher Cu contents. Charge carrier dynamics were studied using time-resolved photoluminescence spectroscopy and revealed drastically suppressed radiative recombination and extended exciton lifetime from ~3 ns in undoped ZAO (or conventional ZAO Air) to >19 ns for Cu-doped variants. The evolution of these synergistic properties with Cu-loading improved the photocatalytic functionality of these materials: Cu-doped ZAO exhibited dramatically enhanced Congo Red photodegradation, while 5–20% Cu-loaded compositions achieved record hydrogen evolution rates among previously reported phase-pure aluminate spinels. The 20% Cu-ZAO photocatalyst showed the best performance under pure visible light (>400 nm) both with and without sacrificial agents, demonstrating excellent applicability for solar-driven water splitting. This work establishes a tunable platform for developing dual-function mesoporous photocatalysts with high surface area for advancing technology in sustainable energy and environmental remediation.

Received 27th February 2026,
Accepted 26th May 2026

DOI: 10.1039/d6nr00820h

rsc.li/nanoscale

1. Introduction

Global energy consumption has experienced a dramatic surge since the industrial revolution.[1] Decarbonizing the global economy across all its diverse sectors necessitates the achievement of net-zero emissions, and this in turn is critically dependent on the development and implementation of clean energy technologies. Presently, fossil fuels constitute the principal global energy source and essential feedstock for manufacturing vital chemical products, including plastics and fertilizers. This fossil fuel dependence has resulted in an escalating atmospheric carbon dioxide concentration, a primary driver of climate change.[2] With both worldwide energy demand and environmental concerns intensifying, developing renewable energy resources independent of fossil fuels and free of carbon dioxide emissions is imperative. Solar energy has gained considerable attention as a sustainable and clean alternative. Within solar energy conversion strategies, solar-driven water splitting stands out as a highly promising method for transforming sunlight into storable hydrogen fuel.[3]

Semiconductor photocatalysts enable photocatalytic water splitting into hydrogen and oxygen, a strategy offering significant potential for converting solar energy into clean, carbon-neutral H_2 fuel through a low-cost and environmentally benign process. This field expanded significantly after Honda and Fujishima's 1972 discovery of photoelectrochemical (PEC) water splitting on a titania electrode.[4] Fundamentally, the overall photocatalytic water splitting reaction comprises three key stages: (i) light absorption by the semiconductor, generating electron–hole pairs; (ii) separation of the charge carriers and their migration towards the semiconductor surface; and (iii) surface reactions involving the charge carriers, producing H_2 or O_2. The overall efficiency of the process hinges on the thermodynamic and kinetic balance across these three stages.[5] Substantial research efforts focus on developing photocatalysts with enhanced solar spectrum absorption (step i) and

[a]EaStChem, School of Chemistry, University of St Andrews, North Haugh, St Andrews, Fife KY16 9ST, UK. E-mail: rtb5@st-andrews.ac.uk; Tel: +44 (0)1334 463899
[b]School of Engineering and Design, London South Bank University, London SE1 0AA, UK. E-mail: sajjadt@lsbu.ac.uk

improved charge separation and migration (step ii). Strategies to broaden light absorption in wide-bandgap semiconductors include bandgap engineering (*e.g.*, by ion doping)[6] and coupling with narrow-bandgap semiconductors (commonly referred to as heterojunctions),[7] dye sensitization,[8] surface plasmonic enhancement,[9] and defect engineering.[10] Additional critical factors for boosting photocatalytic hydrogen generation efficiency involve increasing surface area (*e.g.*, creating porous nanostructures)[11] and employing sacrificial agents.[12]

Given that photocatalytic reactions predominantly occur on catalyst surfaces, maximizing surface area generally enhances photocatalytic activity. Consequently, precise control over photocatalyst particle size and morphology is essential for improving applicability.[13] Oxygen vacancies also critically influence photocatalytic performance. While semiconductors typically require photons of energy exceeding the bandgap energy ($h\nu > E_g$) to generate electron–hole pairs, oxygen vacancies contribute to bandgap narrowing by introducing localized defect states. Surface oxygen vacancies are reported to facilitate charge separation, whereas bulk vacancies may act as recombination sites.[14] In a recent study, we synthesized $ZnAl_2O_4$ exhibiting high specific surface area (344 $m^2\ g^{-1}$, the highest reported for this material), substantial pore volume, and uniform pore size distribution using a self-templated approach.[15] These characteristics are typically associated with hard template-based syntheses. However, template-based methods demand significant resources and time, and successful outcomes depend critically on effective impregnation of the precursor within the template pores. Furthermore, template removal itself presents challenges.[16] Here, we modified the conventional sol–gel citrate synthesis protocol by altering the calcination atmosphere (from air to N_2 with limited O_2 supply). This modification left carbon from the citrate precursor together with the Zn and Al cations uniformly distributed throughout the material. This residual carbon functioned as an *in situ* template, yielding high surface area $ZnAl_2O_4$. The specific surface area increased approximately 15-fold (from 22 to 344 $m^2\ g^{-1}$), significantly enhancing photocatalytic performance for Congo Red dye degradation. Additionally, the oxygen-limited calcination induced oxygen vacancies, reducing the material's band gap.[15] The specific surface area achieved substantially exceeded the recently reported maximum of 73 $m^2\ g^{-1}$ for a templated $ZnAl_2O_4$.[17]

Introducing aliovalent dopants into an oxide framework presents a potent strategy for tailoring its electronic properties and carrier dynamics, sometimes leading to markedly improved photocatalytic efficiency. Doping can strategically shift the Fermi level, suppress deep trap recombination, and prolong charge carrier lifetimes, thereby enhancing photon-harvesting and charge extraction efficiency. Moreover, formation of dopant-induced states within the intrinsic bandgap, combined with incorporation of oxygen vacancies and defect engineering, can extend the frequency range of light absorption and establish favorable pathways for charge transfer, promoting spatial separation of photogenerated electrons and holes. Such modifications can act synergistically and collectively drive significant gains in solar-to-hydrogen conversion efficiency.[2,18,19]

Zinc aluminate ($ZnAl_2O_4$), a spinel (AB_2O_4) with a wide band gap (~3.8 eV[15]), requires bandgap reduction for effective utilization of the solar spectrum. To this end, researchers have doped $ZnAl_2O_4$ with various metal ions: Mn (21.6% bandgap reduction, Cr(VI) photodegradation efficiency increase from 69.38% to 86.39%);[20] Fe (bandgap reduction from 5.1–5.6 eV to 2.04–3.14 eV, achieving ~98% degradation of rhodamine B, methylene blue, methyl orange, and methyl red);[21] Cr (bandgap reduction from 3.66 eV to 3.39 eV);[22] Co (bandgap reduction from 3.04 eV to 2.23 eV);[23] Cd (bandgap reduction from 4.15 eV to 2.67 eV).[24]

This study presents a dual-modification strategy for $ZnAl_2O_4$ (or ZAO) based photocatalysts, targeting both electronic structure and morphological control. Strategic copper doping ($Zn_{1-x}Cu_xAl_2O_4$ or %Cu-ZAO) is employed for band-gap engineering with the aim of enhancing visible-light utilization. Concurrently, a modified sol–gel citrate route featuring controlled calcination under restricted oxygen conditions was used to obtain high surface area mesoporous nanoparticles. The efficacy of the engineered materials is carefully demonstrated through applications in photocatalytic wastewater treatment, *via* photodegradation of Congo Red (CR) dye, and photocatalytic H_2 generation, through water splitting.

2. Experimental

2.1. Synthesis of the material

Mesoporous Cu-doped zinc aluminate nanomaterials were synthesized using a modified sol–gel citrate method.[15] Stoichiometric amounts of precursors, $Zn(NO_3)_2{\cdot}6H_2O$, $Cu(NO_3)_2{\cdot}3H_2O$, and $Al(NO_3)_3{\cdot}9H_2O$, corresponding to the target compositions, $Zn_{1-x}Cu_xAl_2O_4$ (x = 0.01, 0.02, 0.05, 0.1, 0.2), were dissolved in 200 ml of deionized water under continuous stirring for 20 min. Citric acid was introduced into the solution at a molar ratio of 2 : 1 (citric acid : total metal cations). The temperature of the solution was raised to 80 °C and held for 1 h under stirring. Subsequently, the temperature was raised to 120 °C and maintained until the formation of a gel. The resultant gel was dried in a box furnace at 140 °C for 1 h. The dried gel underwent calcination under controlled atmospheres. Samples were first heated under flowing N_2 gas (100 $cm^3\ min^{-1}$) at a rate of 1 °C min^{-1} to 700 °C and kept at this temperature for 2 h. The gas flow was then switched to 0.81% O_2/N_2 (125 $cm^3\ min^{-1}$) for an additional 1 h, followed by cooling to room temperature within the furnace. To ensure complete removal of organics, residual carbon, and nitrates, samples with x = 0.01, 0.02, 0.05, and 0.1 underwent a secondary calcination step in static air at 570 °C for 4 h. The sample with x = 0.2 required heat treatment at 600 °C for 4 h for the same purpose. All secondary calcinations employed heating and cooling rates of 1 °C min^{-1}. The final products are designated as X% Cu-ZAO, where X is the target wt% Cu incorporated, and has values of 2, 5, 10 and 20. For comparative pur-

poses, a reference sample (ZAO-Air) was prepared *via* the conventional sol–gel citrate route. This involved calcination of the dried $ZnAl_2O_4$ gel exclusively in static air at 700 °C for 3 h, using heating and cooling rates of 2 °C min^{-1}.[15,25] Also, an intermediate product of $ZnAl_2O_4$ was prepared under the same conditions as for the %Cu-ZAO samples to allow quantification of the C content in the intermediate phase. This will be referred to as ZAO-intermediate.

2.2. Characterisation

The crystal structure, phase purity, lattice parameters, and crystallite size of the synthesized materials were characterised using powder X-ray diffraction (XRD) on a Panalytical X'Pert instrument. Measurements employed Cu Kα radiation (λ = 1.5405 Å) at 40 kV and 30 mA, scanning a 2θ range from 10° to 90° with a step size of 0.008°.

Fourier transform infrared (FTIR) spectroscopy was performed on a Shimadzu IRAffinity 1S Spectrometer, acquiring spectra over the range of 400–3500 cm^{-1}.

Microstructural analysis utilized a Titan Themis 200 keV (FEI) transmission and scanning transmission electron microscope (S/TEM), equipped with an X-FEG Schottky field emission gun and a spherical aberration corrector. For TEM/STEM examination, samples were dispersed in acetone *via* ultrasonication and deposited onto holey carbon-coated Ni grids. Selected Area Electron Diffractograms (SAEDs), bright field TEM images, and STEM images (including at High Angle Angular Dark Field, HAADF) were recorded. ImageJ software was used for analysis of SAEDs and TEM images. Energy-dispersive X-ray spectroscopy (EDS) analysis was performed for compositional analysis of the samples using the integrated Oxford Instruments X-Max 50 mm^2 detector on the Zeiss Supra 55 VP field-emission scanning electron microscope.

Bulk elemental composition was confirmed by inductively coupled plasma mass spectrometry (ICP-MS) using an Agilent 7900 instrument. Samples underwent nitric acid digestion at 80 °C for 8 h in a closed vessel (Teflon-lined autoclave) and were diluted to ~2% HNO_3 prior to analysis. Calibration utilized matrix-matched multi-element standards, with Rh, Ir, and Sc as internal standards for the correction of drift/matrix effects. Analyses employed Helium collision mode (4.3 mL min^{-1}) to remove polyatomic interference. Quantification of carbon content was performed using CHN elemental analysis on a ThermoFlash 2000 instrument (London Metropolitan University elemental analysis facility).

Specific surface area (BET method) and pore size distribution (BJH method) were determined from N_2 adsorption–desorption isotherms measured on a Tristar Micromeritics-II instrument. Samples underwent degassing at 120 °C overnight prior to analysis.

UV-Visible diffuse reflectance spectroscopy (DRS) spectra of solid samples were recorded on a Jasco V650 spectrometer using a solid sample holder, scanning from 190 to 900 nm. For analysis of solutions from photodegradation experiments, the liquid sample holder was used, scanning from 300 to 650 nm.

X-ray photoelectron spectroscopy (XPS) analysis was performed using a Kratos Axis Ultra DLD photoelectron spectrometer housed in an ultrahigh vacuum chamber (base pressure ~1×10^{-10} mbar). A monochromatic Al Kα X-ray source (1486.6 eV) operating at 15 kV and 4 mA was used. High-resolution spectra were acquired for the Zn 2p, Cu 2p, Al 2p, C 1s and O 1s core levels. Peak fitting was carried out using CasaXPS software (version 2.3.25).

Steady-state photoluminescence (PL) spectra were acquired using an Edinburgh Instruments FLS1000 spectrofluorometer following excitation at 375 nm. Time-resolved PL (TRPL) decays were subsequently recorded using the same instrument equipped with a time-correlated single-photon counting (TCSPC) module. For TRPL measurements, samples were excited using a picosecond pulsed diode laser source (HPL-405, λ_{ex} = 405 nm), and the time-dependent emission was detected at 435 nm using a high-sensitivity visible photomultiplier tube (PMT).

2.3 Photocatalytic evaluation

2.3.1. Photodegradation of congo red. Photodegradation studies employed a homogeneous 20 mg dm^{-3} CR solution prepared in deionized water. For each experiment, 100 ml of this solution was combined with photocatalyst to achieve a concentration of 0.25 g dm^{-3}. The resulting mixture was placed in the reaction chamber and stirred continuously at room temperature throughout the duration of the experiment. The reaction chamber was equipped with a quartz window at the top. The chamber was double-jacketed enabling a continuous flow of water from a Lauda circulation-chiller maintained at 25 °C. Prior to light exposure, the suspension was equilibrated in the dark for 30 min to quantify adsorption of the dye onto the catalyst surface. Subsequently, the solution was subjected to photoirradiation using a 200 W Xenon UV-vis light source. Aliquots were extracted at 10 min intervals for UV-vis spectroscopic analysis to monitor the remaining concentration of the CR dye.

2.3.2. Photocatalytic H_2 production. Photocatalytic hydrogen evolution experiments were conducted at room temperature in a sealed 150 mL photo-reactor with a quartz optical window. All experiments employed 20 mg of photocatalyst dispersed in 50 mL of liquid under continuous stirring at 500 rpm. The temperature was monitored and maintained at 25 °C. Three distinct reaction systems were investigated:

1. Sacrificial agent system: deionized water containing 0.35 M $Na_2S{\cdot}xH_2O$ (Sigma-Aldrich) and 0.25 M Na_2SO_3 (ACS reagent, ≥98.0%, Sigma-Aldrich).

2. Sacrificial agent-free system: pure deionized water without any chemical additives.

3. Alternative system (best catalyst only): a 4 : 1 (v/v) deionized water : methanol mixture was used for the highest performing photocatalyst (without other sacrificial agents).

4. Visible-light systems (best catalyst only): the top-performing photocatalyst was additionally evaluated under visible light

irradiation (>400 nm and intensity equivalent to 1 sun) both with sacrificial agents (0.35 M Na_2S/0.25 M Na_2SO_3) and without sacrificial agents in pure deionized water.

Prior to irradiation, dissolved oxygen and gaseous contaminants were removed by purging the solution with N_2 gas for 30 min to establish an inert atmosphere. The light sources used were:

• UV-Vis light: Oriel LCS-100 solar simulator (Newport) with AM 1.5G filter (Systems 1–3).

• Visible light: ABA LED solar simulator (Newport, LSH-7320) at one sun intensity (400–1100 nm spectrum) (System 4).

Hydrogen evolution was quantified hourly over a 3 h period. Gas samples were extracted using a gas-tight syringe and analyzed by gas chromatography using a Stanford Research International SRI 8610C compact GC. The GC system was equipped with a fused silica capillary column (30 m × 0.53 mm) and a thermal conductivity detector (TCD), with Ar used as the carrier gas.

3. Results

3.1. X-Ray diffraction

Fig. 1 shows the XRD patterns for the synthesized $Zn_{1-x}Cu_xAl_2O_4$ materials. The peaks are indexed to the cubic structure with the *Fd*3*m* space group and unit cell dimension, $a \sim 8.08$ Å (ICSD reference no. 121152,[26] crystallography open database 9013642 and JCPDS code: 93-901-3643). No extra peaks corresponding to any impurities were found in the diffractograms, indicating that all the samples achieved phase purity. Peak broadening in the Cu-doped samples indicates reduced crystallite sizes in these samples compared to the ZAO-Air.

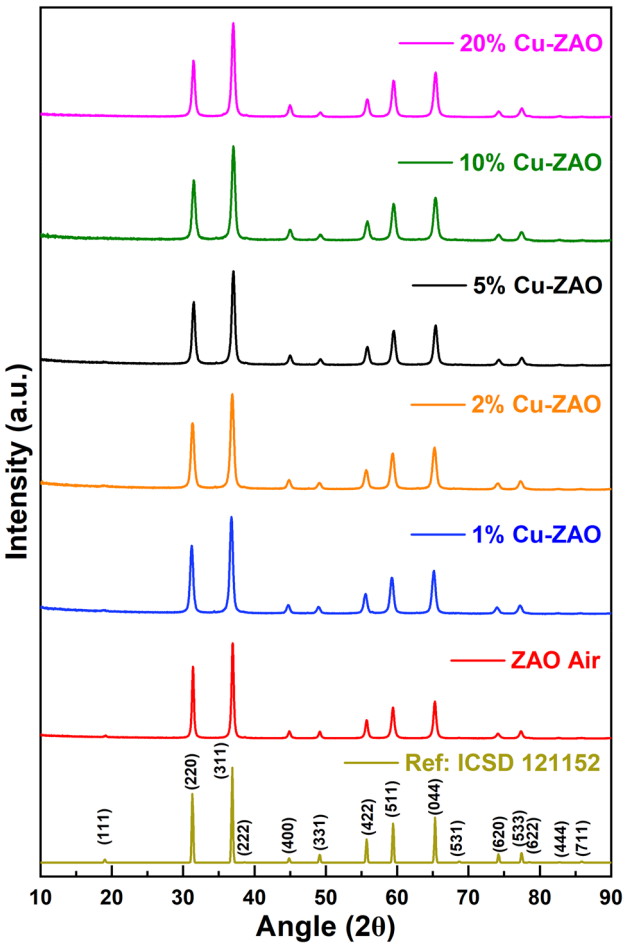

Fig. 1 Stacked X-ray diffractograms for conventional (ZAO Air) and Cu-doped samples, with ICSD reference pattern (ICSD 121152).

Fig. 2(a) shows the Williamson–Hall (WH) plots used to estimate crystallite size and micro-strain.[26] The Cu-ZAO samples were calcined in N_2 with residual carbon from the citrate (that acts as a self-template). For these samples, the XRD peaks are broader (larger FWHM), shifting the WH points upward and producing a higher *y*–intercept, implying smaller crystallite sizes for the Cu-doped ZAO samples. In Fig. 2(b), both Williamson–Hall[27] and Scherrer[28] analyses yield markedly smaller crystallite sizes for Cu-doped ZAO than for the air-calcined material, ZAO-Air, reflecting the self-templating effect of carbon which inhibits crystal growth. This is consistent with the very high BET surface areas (up to 344 $m^2\ g^{-1}$) reported previously for $ZnAl_2O_4$ prepared using the same self-templating method.[15] Notably, in the samples with increasing Cu loading (up to 10%) these ultrafine crystals (~16–17 nm) are maintained, whereas the 20% Cu sample shows a slight increase in crystallite size, which is expected because this material was oxidised at a slightly higher temperature than the others to remove residual carbon. Fig. 2(c) shows that the lattice constant decreases only marginally with increasing Cu content, which is consistent with the fact that the ionic radii of Cu^{2+} (0.73 Å) and Zn^{2+} (0.74 Å) are very similar.[29] Therefore minimal distortion of the spinel framework would be expected on Cu^{2+} for Zn^{2+} substitution.

In Fig. 2(c), lattice constant is seen to fall and then remain approximately constant with increasing %Cu values. We explain this trend with a larger change than expected through several features. As the proportion of Cu^{2+} increases we see an increase in defects. These defects are shown to be predominantly made up of oxygen vacancies through XPS analysis. Lattice expansion due to the presence of oxygen vacancies has been reported and is a widely accepted sign of the presence of oxygen vacancies.[30] An increase in oxygen vacancy concentration on doping Cu^{2+} into a Zn^{2+}-based oxide has been reported.[31] The use of a restricted oxygen supply during calcination in addition to substituting Cu^{2+} for Zn^{2+} (see XPS results below) will both contribute to the formation of oxygen vacancies. This will result in an expansion of the lattice at a greater rate than for substitution alone.

Fig. 2(d) shows the micro-strain extracted from WH plots. The Cu-doped samples exhibit lower strain, which can be attributed to the longer overall heat-treatment duration during preparation (3 h in N_2 and low O_2/N_2, and then 4 h in air for removal) compared to ZAO-Air (3 h in air only). The slight

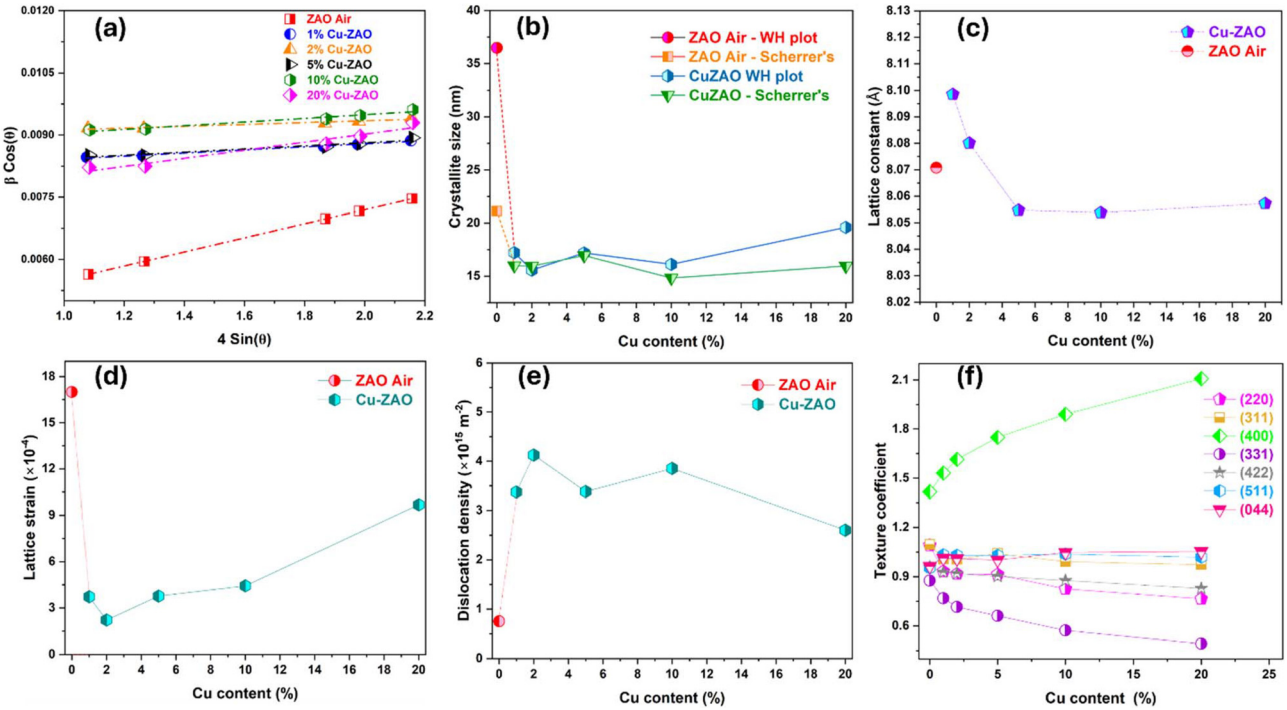

Fig. 2 (a) Williamson–Hall plots, (b) crystallite size, (c) lattice constant, (d) lattice strain, (e) dislocation density and (f) texture coefficients (of selected main planes).

increase in strain for 20% Cu-ZAO compared with the 1–10% Cu-ZAO samples can be attributed to slightly increased crystal growth, as this material was subjected to calcination in air at 600 °C. The dislocation density, calculated using the crystallite sizes obtained from the WH plots and shown in Fig. 2(e), is higher for Cu-ZAO, reflecting its smaller crystallite sizes. This is again a natural consequence of the templated, nanocrystalline morphology. The texture coefficients for major planes are shown in Fig. 2(f). As Cu content increases, the (400) reflection becomes increasingly preferred. Its texture coefficient rises from ~1.41 at 0% Cu to ~2.10 at 20% Cu, indicating enhanced growth normal to the (400) planes. In contrast, the (331) orientation steadily diminishes (from ~0.87 to ~0.49). The (220) and (422) planes show very slight decreases, while other planes remain almost unaffected. In sum, the combined XRD data, together with our previous work using this method to make ZAO materials, strongly indicate that the N_2 treatment is the primary cause of the finer crystals and broader XRD peaks in Cu-ZAO, with additional subtle lattice effects linked to Cu substitution.[15]

Table 1 shows the average crystallite size, lattice constant, lattice strain and the dislocation density extracted using the five most intense, distinct peaks in the XRD diffractograms (corresponding to the planes (220), (311), (422), (511) and (044)). It can be concluded from these calculated parameters that, overall, calcination under N_2/limited O_2 suppresses crystallite growth, leading to smaller XRD-derived crystallite sizes and a more nanostructured spinel than the conventionally synthesized ZAO-Air (this is also in good agreement with the TEM and BET results in sections 3.4 and 3.5 respectively).

3.2. Infra-red spectroscopy

Fig. 3 shows the FTIR spectra of all samples. The $ZnAl_2O_4$ aluminate spinel phase is confirmed by the presence of the bands at ~651.8 (Zn–O), ~547.7 (Al–O), and ~479.6 cm^{-1} (Zn–O–Al), which can be assigned to the ZnO_4 tetrahedra and AlO_6 octahedra of the spinel structure.[32] Corresponding peaks for Cu–O, Al–O and Cu–O–Al are reported for the $CuAl_2O_4$ structure at ~700, ~598 and ~525 cm^{-1}, respectively.[33] As these peaks are somewhat displaced from the positions of the peaks for $ZnAl_2O_4$, they broaden the original peaks, as Cu content increases from zero in the ZAO-Air sample. The weak bands at 2890–2990, 1039–1081 and 2314–2372 cm^{-1} are assigned to C–H, and C–O stretches associated with residual surface carbonaceous material, and to adsorbed atmospheric CO_2.[34,35]

3.3. CHN, EDS and ICP-MS

As revealed by elemental analysis (Table 2), the intermediate product obtained after calcination under low oxygen conditions (0.81% O_2/N_2) retained a substantial carbon fraction of 27 wt%. This significant carbon content originates from the citrate precursor and remains structurally embedded under inert conditions. Upon oxidative removal of carbon through subsequent heat treatment in air, the residual carbon content diminished to negligible levels (<0.2 wt%). The presence of this *in situ* carbon matrix during intermediate-stage processing may have served as a structural template, profoundly influencing the material's evolving morphology and textural pro-

Table 1 Parameters extracted from the XRD data of the synthesized samples, together with mean crystallite size, m_V, from TEM

	Mean crystallite size (nm)					
Sample	WH plot	Scherrer's eqn	m_V (TEM)	Lattice constant (Å)	Lattice strain ($\times 10^{-4}$)	Dislocation density ($\times 10^{15}$ m^{-2})
ZAO Air	36.47	21.12	29.6	8.0707	17.00	0.751
1% Cu-ZAO	17.21	16.00	21.1	8.0985	3.71	3.373
2% Cu-ZAO	15.57	15.94	23.0	8.0801	2.21	4.123
5% Cu-ZAO	17.19	16.95	19.1	8.0547	3.76	3.381
10% Cu-ZAO	16.11	14.83	26.6	8.0538	4.43	3.850
20% Cu-ZAO	19.60	15.95	16.8	8.0572	9.68	2.602

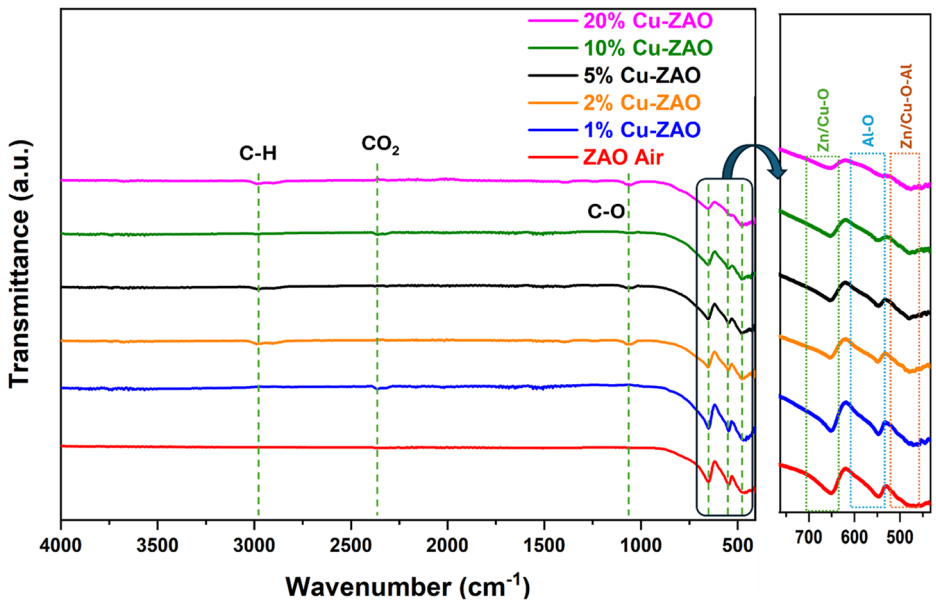

Fig. 3 Stacked FTIR spectra of ZAO-Air and Cu-ZAO samples.

Table 2 Carbon content of the synthesised samples obtained by CHN analysis

Sample	C %
ZAO-intermediate	27
ZAO-Air	0.05
1% Cu-ZAO	0.14
2% Cu-ZAO	0.14
5% Cu-ZAO	0.18
10% Cu-ZAO	0.18
20% Cu-ZAO	0.10

perties. The consequential effects on particle architecture, porosity development, and specific surface area are detailed in the subsequent TEM and BET characterisation sections.

Fig. 4 shows the EDS elemental maps for all samples, in which there is a homogeneous distribution of Zn, Al, O, and Cu. The spatial distributions of elements are consistent with the formation of a single-phase material with Cu fully incorporated into the spinel lattice. The lack of detectable copper-rich domains in the EDS analysis demonstrates that no segregation of Cu-rich phases occurred on the scale of the mapping resolution, underlining the uniformly doped character of these materials. Fig. S1 shows EDS maps of the intermediate product of 10% Cu-ZAO (before C-removal), indicating that the precursors, *i.e.*, Zn, Cu, Al, and O, are homogeneously mixed in the carbon.

The comparison of Zn, Al and Cu atomic percentages obtained from EDS and ICPMS with the theoretical values is presented in Table 3. For the undoped ZAO Air reference material, both EDS and ICP-MS analyses return Zn and Al percentages within 1–2% of the theoretical molar ratio, with negligible Cu detected. In the Cu-substituted $Zn_{1-x}Cu_xAl_2O_4$ series, however, the EDS values diverge from the expected theoretical values. EDS consistently records copper levels higher than the nominal values. EDS is accepted to be only a semi-quantitative method. Therefore, to resolve this difference and examine these compositions in more detail, we employed ICP-MS, which determines the elemental composition of the entire bulk solid (after digestion). As seen in Table 3, this method consistently yields values which are much closer to the intended stoichiometry, confirming that the target compositions were achieved.

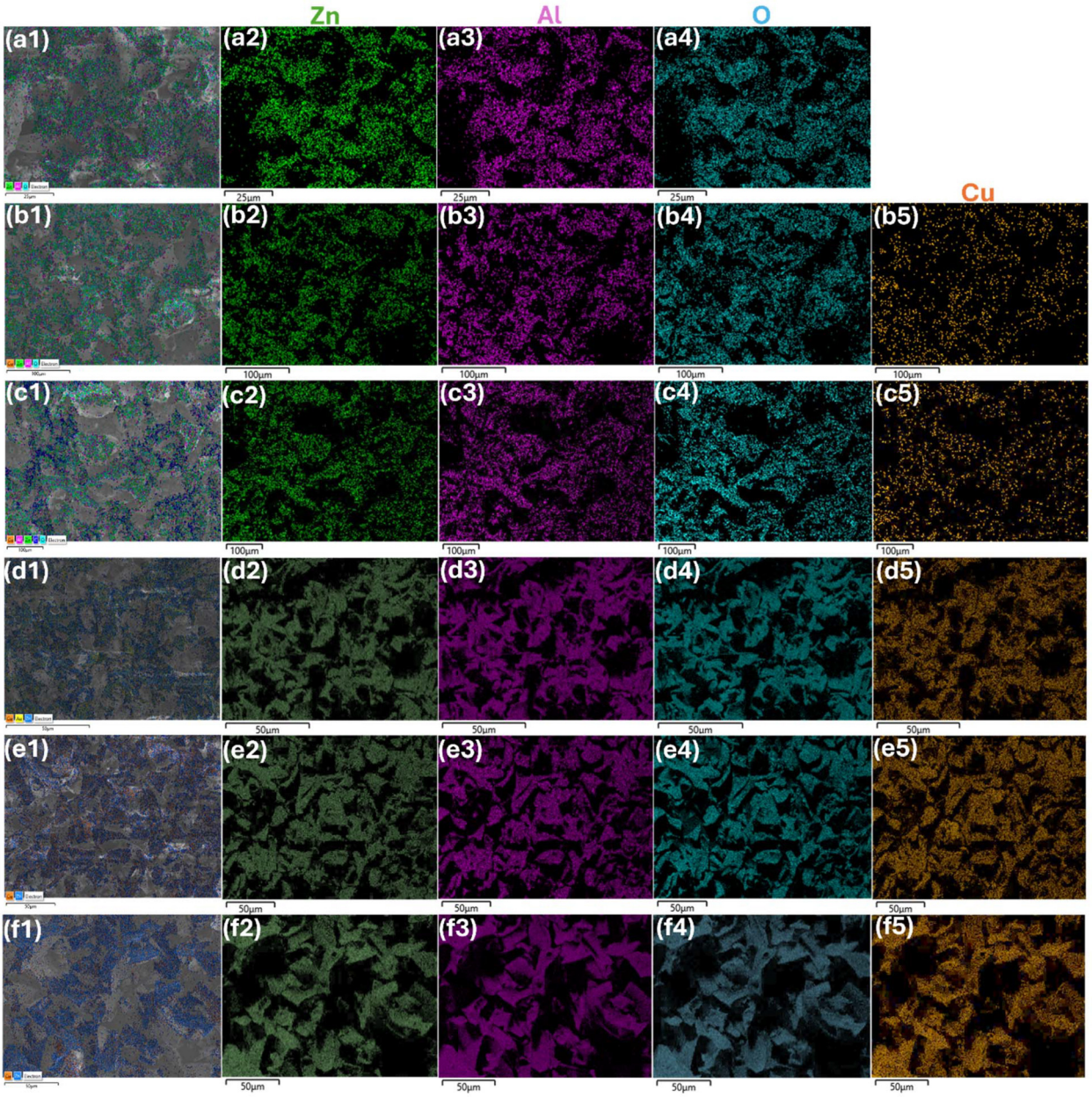

Fig. 4 EDS elemental maps of the samples: (a1–a4) ZAO-Air, (b1–b5) 1% Cu-ZAO, (c1–c5) 2% Cu-ZAO, (d1–d5) 5% Cu-ZAO, (e1–e5) 10% Cu-ZAO and (f1–f5) 20% Cu-ZAO.

Table 3 Cation percentages of Zn, Cu and Al from EDS and ICPMS compared with theoretical values

	Theoretical			EDS			ICPMS		
Sample	Zn %	Cu %	Al %	Zn %	Cu %	Al%	Zn %	Cu %	Al %
ZAO Air	33.3	0	66.7	31.6	0	68.4	33.2	0	66.8
1% Cu-ZAO	33.0	0.333	66.7	32.1	0.788	67.2	31.4	0.431	68.2
2% Cu-ZAO	32.7	0.667	66.7	32.8	0.780	66.4	31.7	0.686	67.6
5% Cu-ZAO	31.7	1.67	66.7	30.6	3.17	66.2	30.3	1.70	68.0
10% Cu-ZAO	30.0	3.33	66.7	29.5	5.48	65.1	29.1	3.37	67.5
20% Cu-ZAO	26.7	6.67	66.7	27.5	11.0	61.6	27.0	7.49	65.5

3.4. TEM

Fig. 5 presents TEM images of all samples taken at intermediate and high magnifications. All materials are composed of roughly spherical, rounded, rather than angular, crystallites. However, there is a marked difference between the conventionally-prepared undoped material and the Cu-doped materials prepared under restricted oxygen conditions. In the images of

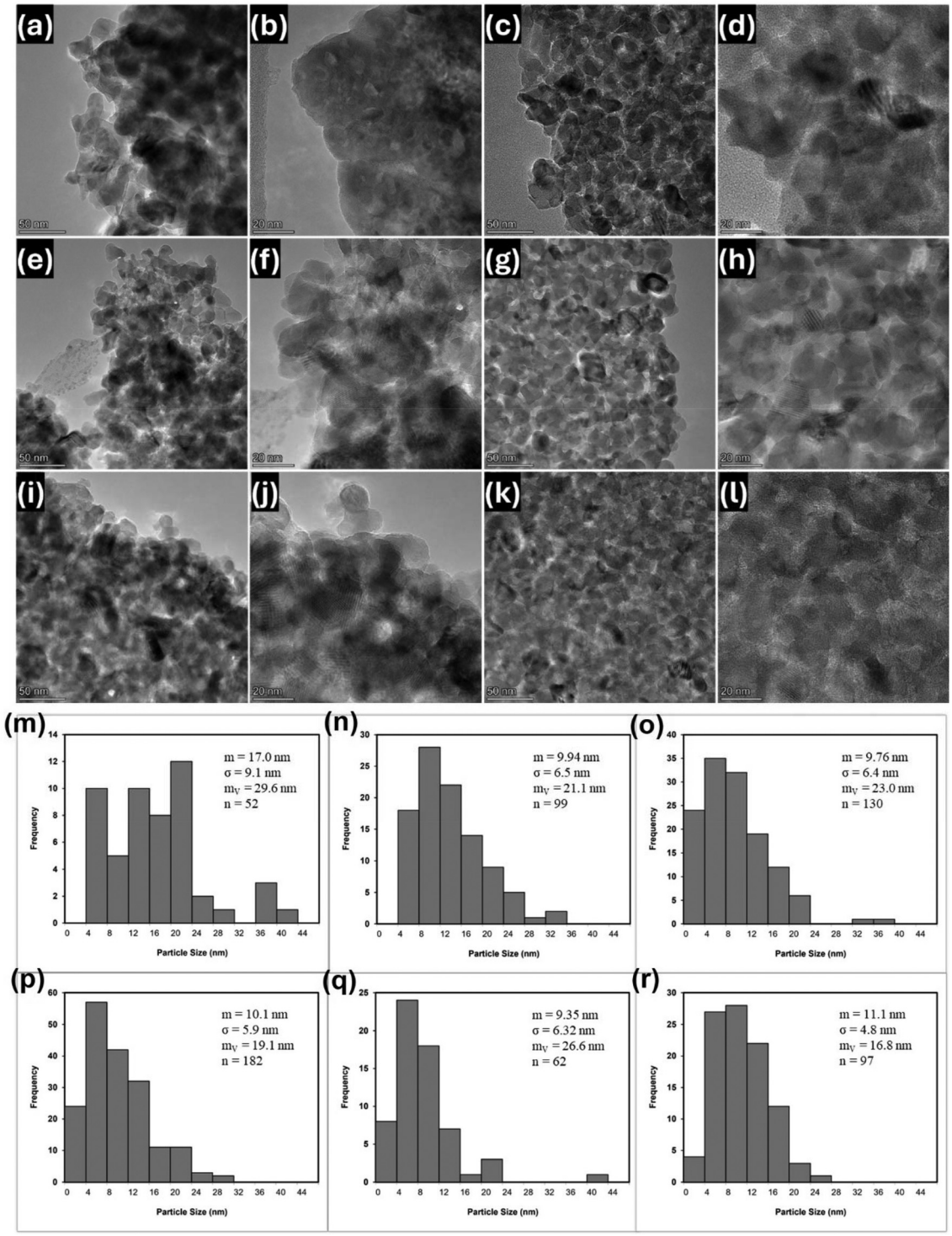

Fig. 5 TEM images recorded at the same two magnifications of the samples: (a and b) ZAO-Air, (c and d) 1% Cu-ZAO, (e and f) 2% Cu-ZAO, (g and h) 5% Cu-ZAO, (i and j) 10% Cu-ZAO and (k and l) 20% Cu-ZAO; and crystallite size distributions obtained from the TEM images for: (m) ZAO-Air, (n) 1% Cu-ZAO, (o) 2% Cu-ZAO, (p) 5% Cu-ZAO, (q) 10% Cu-ZAO and (r) 20% Cu-ZAO. Mean crystallite size, m, standard deviation, σ, volume-corrected crystallite size, m_V, and sample size, n, are inset.

ZAO-Air synthesized in air *via* the standard citrate sol–gel route (Fig. 5(a and b)) the crystallites are relatively large and densely packed resulting in a low external surface area (confirmed in BET results, Table 4, below). By contrast, panels (c–l) show the series of Cu-doped ZAO spinels calcined under N_2 gas atmosphere with a limited supply of oxygen. These all exhibit a much more open structure containing numerous mesopores as well as that the crystallites were generally smaller than for ZAO-Air. To quantify this difference, images of each sample taken at the same magnification were analysed to obtain a large number of crystallite diameters. Crystallite size distribution histograms were plotted and these are presented in Fig. 5(m–r) for each material. Mean crystallite size on both a numerical (m) and volume-adjusted (m_V) basis are inset in the figure panels together with the standard deviation (σ) and sample size (n). The conventionally-prepared ZAO-Air does indeed show a clearly larger mean crystallite size than the other materials (m = 17.0 nm), while the values for all Cu-doped materials are similar to each other (m = 9.35–11.1 nm). The mean weighted to account for crystallite volume, m_V, shows a similar trend, although at higher values, and is included in Table 1. The anomalously high value for 10% Cu in Fig. 5(q) is explained by the presence of a single very large crystallite in the distribution. Accepting this, the trends in m and m_V between samples are qualitatively similar to those determined from the XRD data (Table 1). The most reasonable comparison of these XRD data is with m_V, whose values are in very good agreement. The value of m_V for ZAO-Air is intermediate between those determined by the Scherrer and by the WH approaches. During calcination, carbon released from citrate appears to restrain crystallite growth, directing the formation of a highly dispersed network of nanocrystals within an open, porous framework. This structure and unique morphology are directly responsible for boosting the surface area from 22 m^2 g^{-1} in the air–calcined material to 88 m^2 g^{-1} in the N_2–calcined samples. At a Cu loading of 20% there is no evidence of particle coarsening or phase segregation. XRD peak broadening and TEM analysis confirm that all Cu-substituted samples possess substantially reduced crystallite dimensions compared to the ZAO-Air. The combination of uniform nanocrystals and an interconnected porous architecture gives these materials unique textural properties. These make them especially well-suited for catalytic/photocatalytic and electrochemical applications where high surface to volume ratio and efficient mass transport are critical for the efficiency of the system. In combination with the high surface areas and fine crystallite sizes observed by TEM and BET, the uniform elemental distribution (as shown in EDS) also underscores the effectiveness of our synthetic strategy for producing catalytically active, structurally robust spinels.

Fig. 6 presents the analysis of SAED patterns and high resolution (HR)TEM images for each sample composition. In the SAEDs the interplanar spacings derived from the visible diffraction rings were all successfully indexed to the Miller indices of the cubic $ZnAl_2O_4$ crystal structure (ICSD no. 121152 (ref. 26)), from the 111 planes (~4.66 Å) to the 440 planes (~1.42 Å). There was no evidence of impurity phases. HRTEM images for all samples are presented in Fig. 6(b) and several families of planes were identified from their d spacings in each. The most commonly viewed were the 220 and 311 planes (~2.86 and 2.44 Å, respectively). These images also emphasise the small size of the crystallites of the Cu-doped samples, their highly crystalline nature and the presence of mesopores of apparently uniform size between the crystallites.

3.5. BET

Fig. 7(a) shows the N_2 physisorption isotherms for the intermediate material (with the carbon not yet removed) and the final product of 20% Cu-ZAO together with a comparison of their BET specific surface area and specific pore volume (panel (a) inset). The quantity of N_2 adsorbed on the surface of the intermediate product is negligible compared to the final product. This is a clear indication that the carbon is acting as a self-template since the BET surface area of the intermediate is only 0.47 m^2 g^{-1} (and specific pore volume, 0.000172 cm^3 g^{-1}) but this increases to 72.26 m^2 g^{-1} (and specific pore volume, 0.168 cm^3 g^{-1}) upon carbon removal. Fig. 7(b) compares the N_2 physisorption isotherms for all samples. This shows the difference between the ZAO-Air material and the Cu-doped materials prepared using the modified citrate method. All adsorption isotherms correspond to Type IV(a) according to the classifications of the International Union of Pure and Applied Chemistry, and they exhibit hysteresis loops indicative of capillary condensation within mesopores. The onset of hysteresis occurs at pore widths exceeding a system- and temperature-dependent critical value: in this case, for nitrogen adsorption at 77 K in cylindrical pores, hysteresis starts at widths greater than approximately 4 nm. These hysteresis loops are

Table 4 BET surface area, average pore width and specific pore volume data extracted from the N_2 physisorption isotherms

Sample	BET surface area (m^2 g^{-1})	Crystallite size from XRD – WH plots (nm)	Avg. pore width (nm)		Avg. pore volume (cm^3 g^{-1})	
			Adsorption	Desorption	Adsorption	Desorption
ZAO-Air	22.55	36.47	17.18	12.76	0.103	0.110
1% Cu-ZAO	60.90	17.21	8.20	6.99	0.153	0.164
2% Cu-ZAO	76.25	15.57	6.85	6.03	0.150	0.164
5% Cu-ZAO	88.77	17.19	5.80	5.26	0.166	0.174
10% Cu-ZAO	74.27	16.11	7.56	6.84	0.184	0.198
20% Cu-ZAO	72.26	19.60	6.83	6.03	0.160	0.175

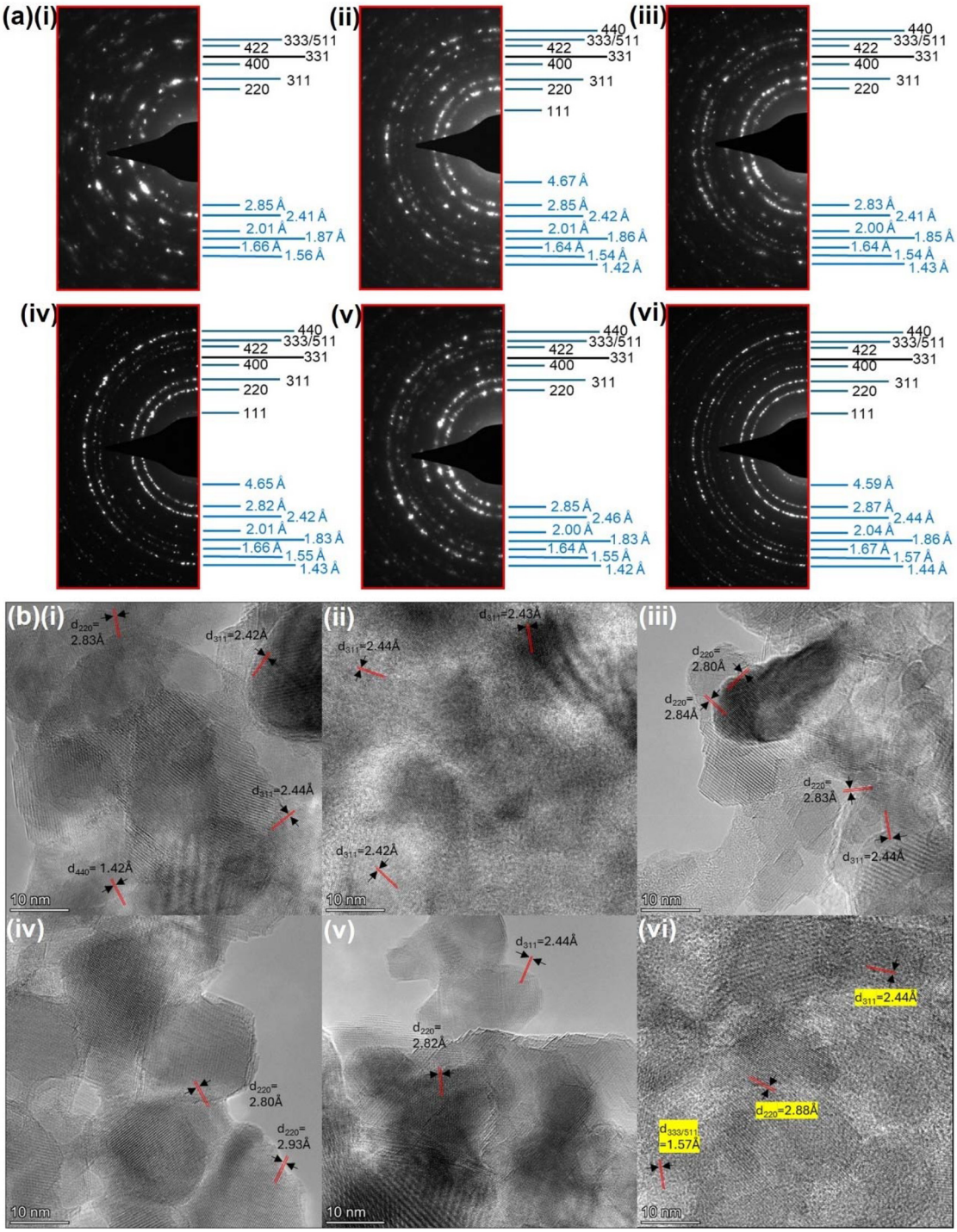

Fig. 6 (a) Selected area electron diffractograms with Miller indices and corresponding interplanar spacings indicated for: (i) ZAO-Air, (ii) 1% Cu-ZAO, (iii) 2% Cu-ZAO, (iv) 5% Cu-ZAO, (v) 10% Cu-ZAO and (vi) 20% Cu-ZAO; (b) High Resolution TEM images with interplanar spacings, *d*, indicated for: (i) ZAO-Air, (ii) 1% Cu-ZAO, (iii) 2% Cu-ZAO, (iv) 5% Cu-ZAO, (v) 10% Cu-ZAO and (vi) 20% Cu-ZAO.

H2-type, characteristic of materials possessing complex pore networks. This loop shape is commonly observed in porous glasses (*e.g.*, Vycor), silica gels, and comparator mesoporous materials SBA-16 and KIT-5.[36] Fig. 7(c) shows the pore size distribution for all samples. ZAO-Air has a wider pore size distribution with its maximum at ~23.7 nm while the Cu-doped samples synthesised *via* the modified sol–gel technique, have narrow-pore size distributions with maxima in the range 7–10 nm. Fig. 7(d) compares the BET specific surface areas and pore widths for all the samples. Table 4 shows the BET

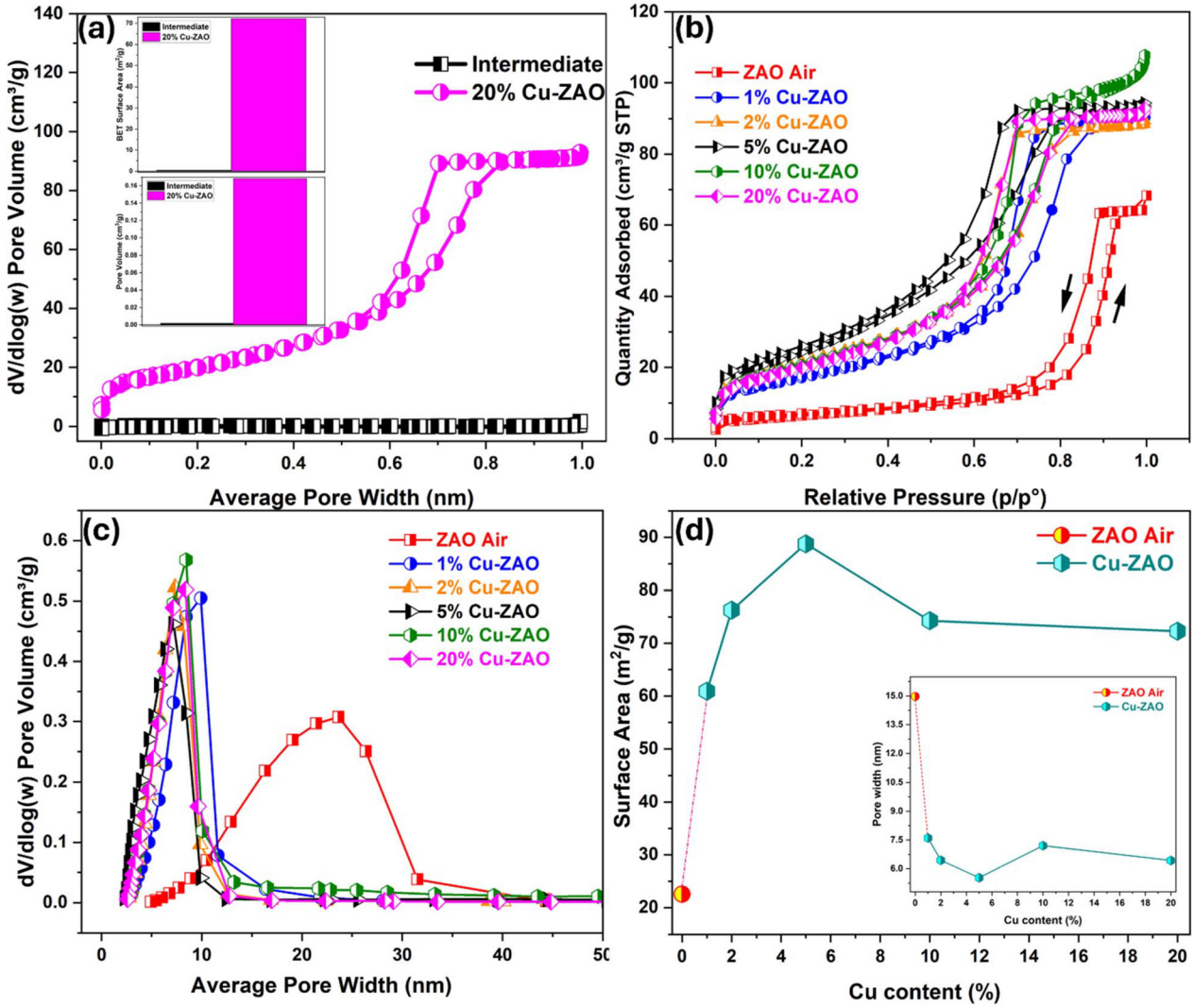

Fig. 7 (a) N_2 physisorption isotherms of intermediate and 20% Cu-ZAO (bar graphs inset compare specific surface areas and specific pore volumes); (b) isotherms for all samples; (c) pore size distribution and (d) surface area trend with %Cu loading. Variation of average pore width with %Cu is inset in (d).

surface area, pore width and pore volume values extracted from the N_2 physisorption data for all the samples. The surface area increases from 22.5 $m^2\ g^{-1}$ for ZAO-Air to 60–88 $m^2\ g^{-1}$ for the Cu-containing materials made by the modified citrate method. The average pore width for ZAO-Air is 15.0 nm which decreases to 5.5–7.6 nm for the Cu-ZAO samples. Overall, the results show that samples prepared using the modified citrate method possessed consistently high specific surface areas as well as narrow pore size distributions.

3.6. XPS

Fig. 8 shows the XPS analysis of the samples. The XPS spectra show the expected features for Zn, Al and O, and emerging Cu signals, for the $Zn_{1-x}Cu_xAl_2O_4$. This confirms that Cu has been successfully incorporated into the matrix. With progressively increasing Cu content, the Zn $2p_{3/2}$ line shifts from ~1021.81 eV (ZAO-Air) to 1021.67 eV (20% Cu-ZAO). This is consistent with an increase in electron density at Zn sites with increasing %Cu.[37] The Cu feature (Fig. 8(c)) appearing around 928–938 eV is characteristic of $2p_{3/2}$ with the main deconvoluted peak assigned to Cu^{2+} and characteristic of spinel structures.[38–43] The smaller deconvoluted peak in the region 932.2–932.8 eV can be attributed to Cu^+ and/or Cu^0 as it is difficult to distinguish between them.[43] However, literature reports show that a portion of Cu^{2+} also sits in octahedral sites of $Zn_{1-x}Cu_xAl_2O_4$ and its d^9 electronic configuration induces a strong Jahn Teller distortion that elongates and weakens certain Cu–O bonds, creating local strain. That strain, together with the partial stabilization of Cu^+ under low temperature or reducing synthesis conditions, lowers the energy required to remove nearby oxygen so oxygen vacancies form to relieve strain and maintain the charge balance.[44] The Al 2p peak also moves to a lower binding energy with increasing %Cu. This represents lattice distortion and a higher local electron density around Al

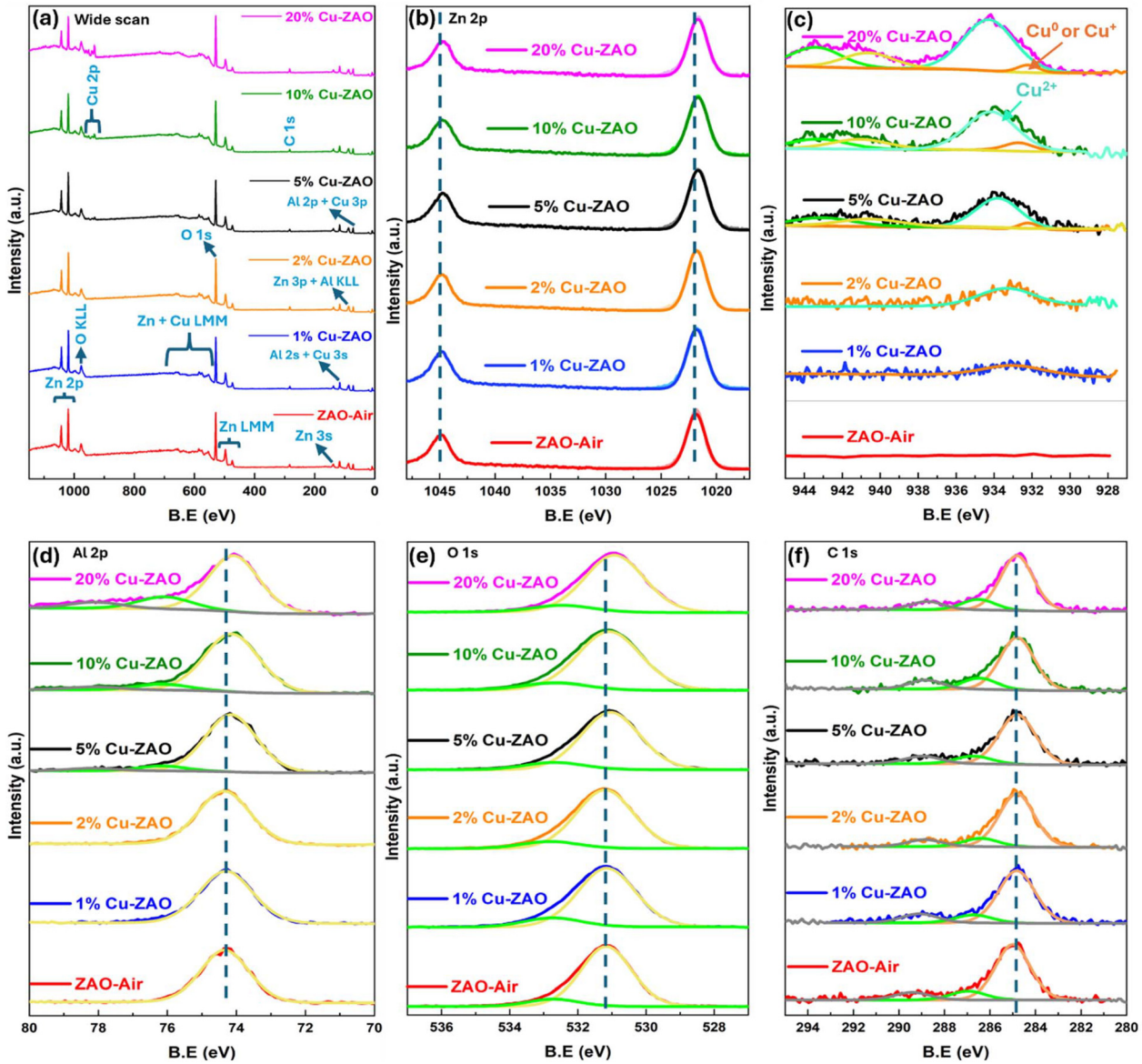

Fig. 8 XPS spectra for all samples: (a) wide scan survey; (b) Zn 2p; (c) Cu 2p; (d) Al 2p; (e) O 1s and (f) C 1s regions.

as oxygen vacancies accumulate.[45] The O 1s feature is deconvoluted into two peaks. The lower intensity peak at 532.4–532.7 eV corresponds to chemisorbed oxygen species while the main peak in the range 530.9–531.18 eV corresponds to lattice oxygen.[15,43] Crucially, the lattice oxygen 1s peak (Fig. 8(e)) shifts with increasing Cu doping from ~531.18 for ZAO-Air to lower B.E., ~530.95 eV, for 20% Cu-ZAO. This can also be attributed to increased oxygen deficiency in the lattice.[45,46] Fig. 8(f) shows C 1s peaks at 289.4, 286.9 and 285.3 eV which correspond to C=O and C–O environments and to sp^3 carbon, respectively. This relates to the small amount of carbonaceous material remaining from the preparation and concentrated at the sample surfaces.[15] In summary, Cu insertion into $ZnAl_2O_4$ produces additional oxygen vacancies. This increases the electron density around Zn and Al and causes Zn 2p and Al 2p to move to a lower B.E. The Cu 2p binding energy remains characteristic of Cu^{2+}, with little or no contribution from Cu^{+}. Simultaneously, the main O 1s peak shifts to lower B.E. due to the higher vacancy concentration. Considering the origin of these oxygen vacancies, Cu^{2+} and Al^{3+} are reported to prefer the octahedral cation sites in $ZnAl_2O_4$ and related spinels.[43] Therefore, despite the target stoichiometry of $Zn_{1-x}Cu_xAl_2O_4$, a proportion of the Cu^{2+} dopant ions might be expected to replace some Al^{3+} on these octahedral sites during synthesis. Such an aliovalent Cu^{2+} for Al^{3+} substitution would decrease the total positive charge in the compound. To maintain electroneutrality, fewer O^{2-} ions would be present in the lattice, forming additional oxygen vacancies, the concentration of which would increase with increasing %Cu. As discussed below, these oxygen vacancy defects may be responsible for the

progressive decrease in band gap (section 3.7), and in the increasing photocatalytic activity (sections 3.9 and 3.10), of these materials as Cu content increased. Quantitative XPS analysis of Zn, Cu, and Al was used to calculate the surface Cu/(Zn + Cu + Al) ratio for all samples (Fig. S2). The XPS data indicate a higher near-surface Cu fraction in the Cu-doped samples, consistent with Cu surface enrichment. In contrast, ICP-MS shows that the bulk compositions remain close to the nominal stoichiometric ratios. This surface enrichment of Cu is expected to influence the photocatalytic performance by modifying the surface electronic structure and providing active sites for charge transfer.

3.7. Diffuse reflectance spectroscopy

The UV–visible diffuse reflectance spectra of the ZAO-Air and Cu-doped ZAO powders, plotted as percentage reflectance, R, *vs.*, wavelength (inset) and transformed into absorbance, are shown in Fig. 9(a). With increasing Cu content, the overall absorbance steadily rises, particularly in the visible region. Whereas the undoped ZAO-Air sample absorbs almost exclusively below 300 nm, the Cu-doped samples show enhanced absorbance at longer wavelengths, particularly above 400 nm, as indicated by the arrow. Such enhanced visible-light harvesting is highly desirable for solar-driven photocatalysis.

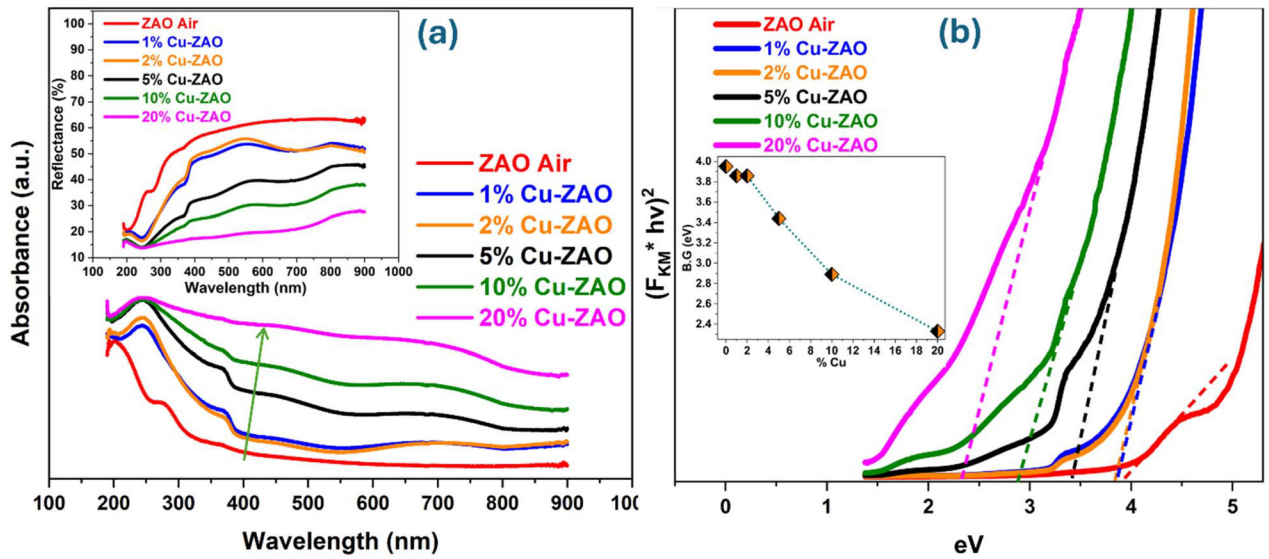

Fig. 9 UV-visible spectroscopy plots: (a) absorbance spectra, with reflectance spectra shown in the inset, and (b) corresponding Kubelka–Munk plots used to extract the band-gap values, with BG *vs.* %Cu shown in the inset.

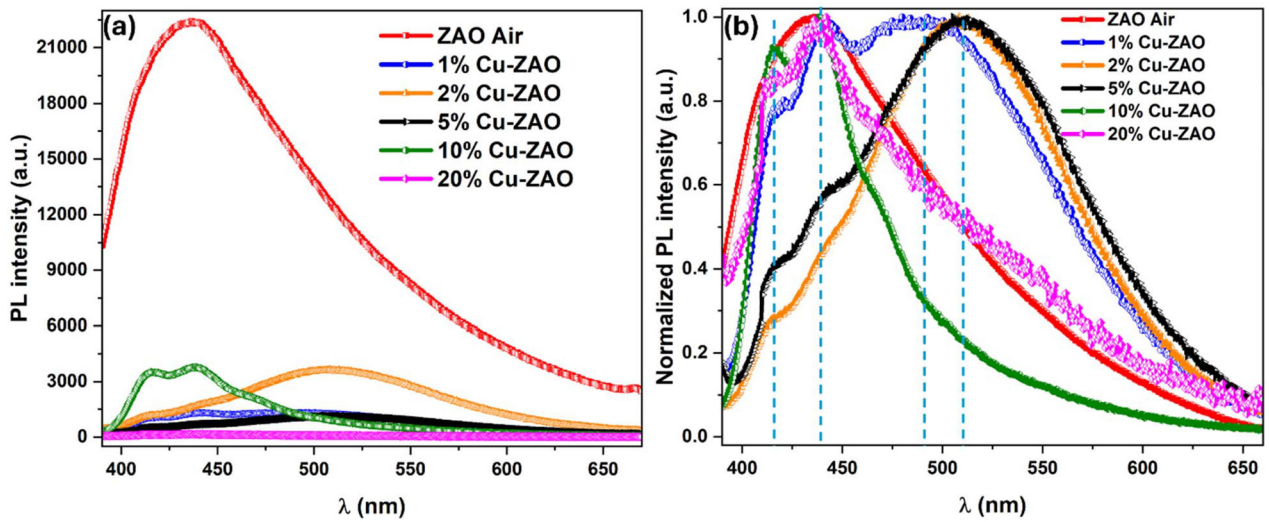

Fig. 10 Steady-state photoluminescence (PL) emission of the synthesised samples: (a) raw PL intensities and (b) normalized PL intensities.

The corresponding graphs of the Kubelka–Munk function[15,47] are given in Fig. 9(b). Extrapolation of the linear regions to the energy axis yields optical band–gap values that decrease progressively with Cu loading: 3.95 eV for ZAO-Air, 3.86 eV for 1% Cu-ZAO, 3.85 eV for 2% Cu-ZAO, 3.44 eV for 5% Cu-ZAO, 2.89 eV for 10% Cu-ZAO and 2.33 eV for 20% Cu-ZAO. The narrowing of the band gap shifts the absorption threshold from the deep UV into the visible region, which is expected to enhance photocatalytic activity under natural sunlight. Fig. S3 shows the band-edge potentials calculated from the XPS-derived valence band positions and the optical band gaps, indicating that Cu incorporation modulates the electronic structure of the samples. The band edges shift with Cu content, which can influence the thermodynamic driving force for photocatalytic reactions. With increasing Cu content, the conduction band shifts to more negative potentials up to about 10% Cu, while the valence band shifts to less positive potentials, consistent with progressive band-gap narrowing. However, the overall photocatalytic performance also depends on other factors such as charge separation efficiency, carrier lifetime, recombination rate, *etc*.

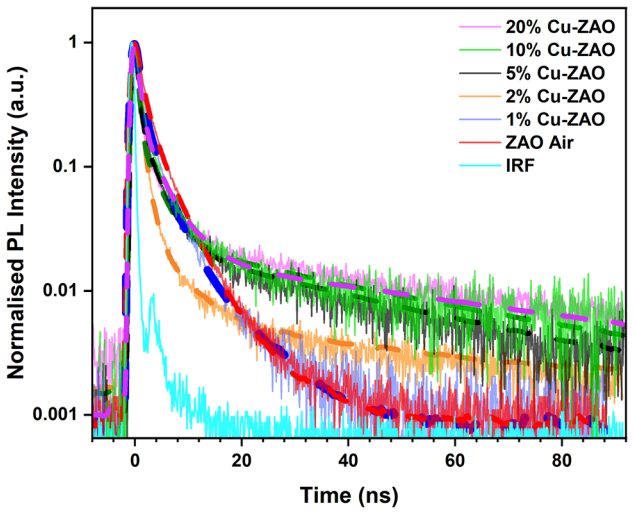

Fig. 11 TRPL decay profiles for the synthesised samples (along with the instrument response function, IRF).

3.8. Photoluminescence (PL) and time-resolved photoluminescence (TRPL)

Fig. 10(a) and (b) show the raw and normalized intensity PL intensity spectra, respectively. The PL emission spectrum of ZAO-Air shows peaks at ~413 nm and ~439 nm, which is consistent with previous studies.[48] Low Cu doping (1–5%) introduces new defect (or "mid-gap") states, narrowing the bandgap and red-shifting the emission peak while at the same time drastically reducing its intensity due to new non-radiative traps (such as oxygen vacancies, as shown in Fig. 8). Doping levels of 10–20% suppress these low-energy emissions, causing the PL to blue-shift relative to the 5% Cu sample and remain very weak due to concentration quenching. The absolute PL intensity decreases from ZAO-Air to the high surface area Cu-doped samples as the defect concentrations increase with Cu content. These trends imply that Cu doping enhances visible-light absorption (*via* mid-gap states and E_g narrowing), while reducing radiative carrier recombination. For photocatalysis, this means more effective charge separation and reduced radiative recombination, both of which are desirable for enhanced photocatalytic efficiency.

The TRPL decay profiles measured for these materials are presented in Fig. 11. These profiles were fitted using a biexponential function to extract the intensity-weighted mean lifetime, τ_{int}, for each material. The ZAO-Air reference sample exhibited a τ_{int} of 3.15 ns. Introducing 1% Cu slightly increased τ_{int} to 3.85 ns, suggesting the formation of shallow traps that capture carriers before recombination and thereby

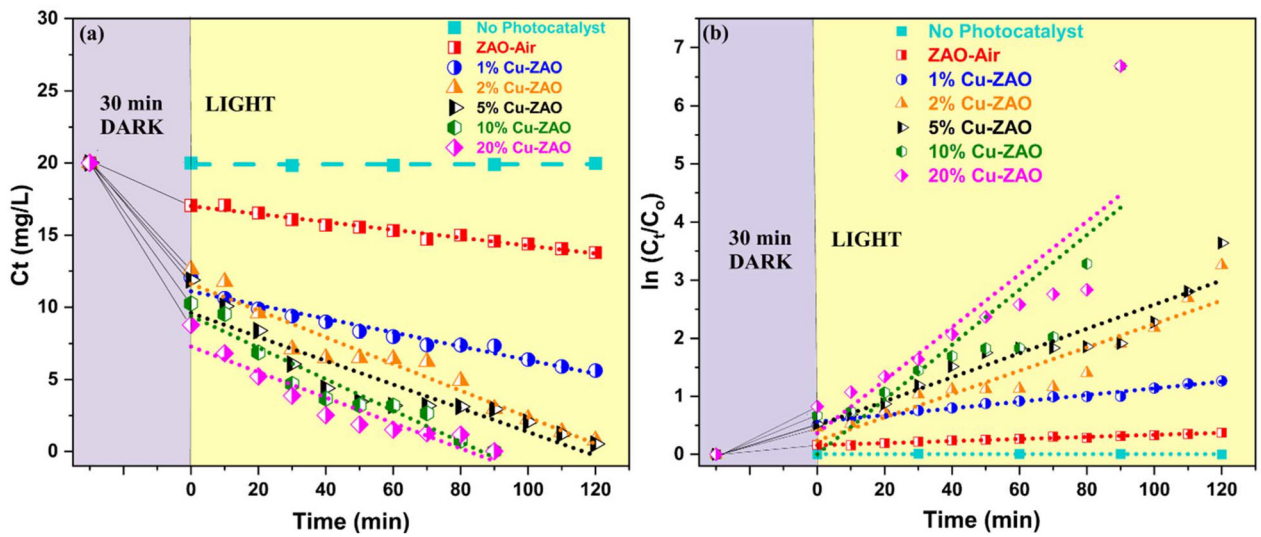

Fig. 12 Kinetics of the CR photodegradation: (a) zero-order kinetics and (b) first-order kinetics.

prolong emission. At 2% Cu, τ_{int} decreased to 2.90 ns, indicating the presence of traps associated with faster recombination pathways than those present at 1% Cu. In contrast, higher Cu concentrations (5–20%) led to a steady increase in τ_{int}: 13.96 ns at 5%, 17.04 ns at 10%, and 19.45 ns at 20%. These longer lifetimes indicate the formation of deep traps that retain photogenerated carriers for extended durations. This improvement in carrier lifetime correlates directly with the improvement in photocatalytic H_2 evolution (as shown in Fig. 13). This confirms that enhanced charge separation, facilitated by deep traps, is the primary driver of improved photocatalytic performance in Cu-doped ZAO.

Table 5 Fit quality (R^2) and apparent rate constants (k_0 and k_1) from the photodegradation of CR

	Zero order kinetics		First order kinetics	
Sample	R^2	k_0 (mg dm^{-3} min^{-1})	R^2	k_1 (min^{-1})
ZAO Air	0.973	$0.027 \pm 1.38 \times 10^{-3}$	0.977	$0.002 \pm 8.15 \times 10^{-5}$
1% Cu-ZAO	0.957	$0.048 \pm 3.05 \times 10^{-3}$	0.977	$0.006 \pm 2.66 \times 10^{-4}$
2% Cu-ZAO	0.943	$0.092 \pm 6.85 \times 10^{-3}$	0.869	$0.020 \pm 2.34 \times 10^{-3}$
5% Cu-ZAO	0.856	$0.082 \pm 1.02 \times 10^{-2}$	0.895	$0.021 \pm 2.14 \times 10^{-3}$
10% Cu-ZAO	0.925	$0.109 \pm 1.10 \times 10^{-2}$	0.655	$0.047 \pm 1.21 \times 10^{-2}$
20% Cu-ZAO	0.900	$0.089 \pm 1.04 \times 10^{-2}$	0.693	$0.046 \pm 1.07 \times 10^{-2}$

3.9. Photocatalytic dye degradation

The photodegradation of CR was quantitatively evaluated under UV-visible light irradiation by monitoring its concentration (as shown in Fig. S4) and fitting the results to both zero- and first-order kinetic models, as shown in Fig. 12 and summarised in Table 5. The Cu-doped variants exhibit higher CR adsorption before illumination. This is attributed to the high surface areas compared to ZAO-Air. The ZAO-Air sample shows relatively sluggish kinetics (k_0 = 0.027 mg dm^{-3} min^{-1}; k_1 = 0.0020 min^{-1}), whereas 1% Cu doping enhances the apparent rate constants (k_0 = 0.047 mg dm^{-3} min^{-1}, k_1 = 0.0058 min^{-1}). Further increasing the Cu content to 2% and 5% in Cu-ZAO leads to a continued rise in degradation rate (k_0 up to 0.092 and 0.082 mg dm^{-3} min^{-1}; k_1 up to 0.0201 and

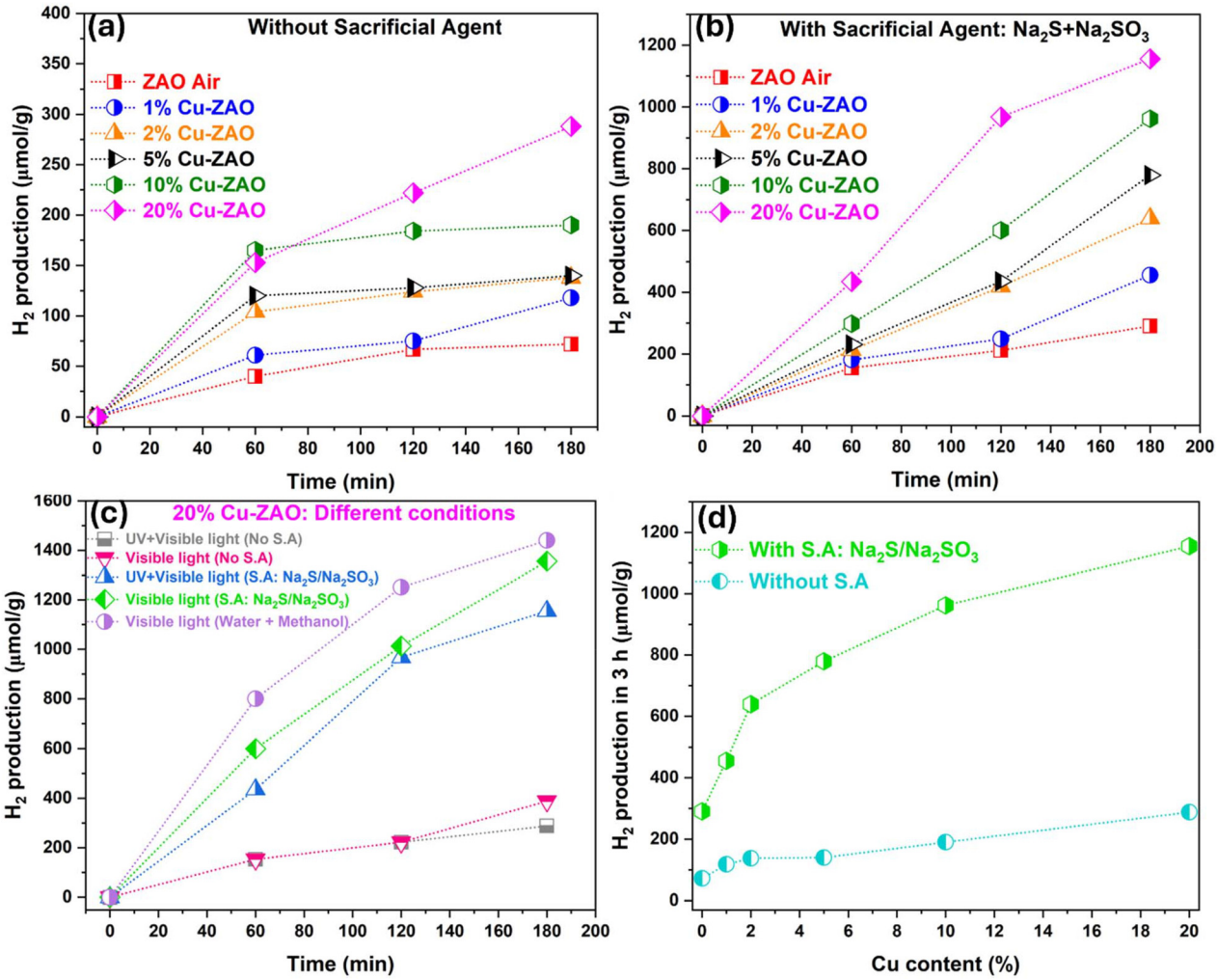

Fig. 13 Photocatalytic H_2 production: (a) without sacrificial agent; (b) with sacrificial agent; (c) with 20% Cu-ZAO in different conditions, and (d) trends with Cu concentration.

0.0208 min^{-1}, respectively), demonstrating a strong correlation between Cu loading and photocatalytic activity. The 10% Cu-ZAO sample attains the highest zero-order decolorization rate (k_0 = 0.109 mg dm^{-3} min^{-1}) and a first-order rate constant of 0.0472 min^{-1}, whereas 20% Cu-ZAO also delivers high performance (k_0 = 0.088 mg dm^{-3} min^{-1}; k_1 = 0.0456 min^{-1}), confirming that copper incorporation in the 10–20% range effectively enhances CR degradation without significant loss of activity at these higher loadings.

Fig. S5 presents the reusability performance of 20% Cu-ZAO over three consecutive degradation cycles. The same sample was subjected to repeated photocatalytic tests; following complete decolourisation of the CR solution in the first cycle, the catalyst was kept under UV irradiation with continuous stirring for an additional 30 min, then thoroughly dried and reused with a fresh CR solution (20 mg dm^{-3}). The material retained high activity, achieving ~98.5%, ~95.8%, and ~94.5% decolourisation after 30 min of UV exposure in the first, second, and third cycles, respectively.

3.10. Photocatalytic hydrogen generation

The photocatalytic H_2 evolution performance of ZAO-Air and Cu-ZAO spinels, both in the presence and absence of a sacrificial agent, is summarized in Fig. 13, and the quantities of H_2 produced are included in Table 6. In the absence of any sacrificial reagent (panel a), increasing Cu loading markedly enhances H_2 production: ZAO-Air yields 72 μmol g^{-1} after 3 h, while 1 to 20% Cu-ZAO deliver 118 to 288 μmol g^{-1}, respectively. Introduction of Na_2S/Na_2SO_3 as a dual sacrificial agent (panel b) further amplifies activity, with H_2 outputs of 290 μmol g^{-1} for ZAO-Air and 456–1155 μmol g^{-1} for the 1–20% Cu-ZAO series, after 3 h. For 20% Cu-ZAO, the best-performing sample (panel c), combined UV-visible irradiation without a sacrificial agent produced 180 μmol g^{-1} H_2 (60 μmol h^{-1} g^{-1}). This increased to 288 μmol g^{-1} (96 μmol h^{-1} g^{-1}) under visible light alone and reached 388 μmol g^{-1} (129 μmol h^{-1} g^{-1}) under UV-visible radiation with Na_2S/Na_2SO_3. Remarkably, pure visible–light irradiation with Na_2S/Na_2SO_3 yielded 1155 μmol g^{-1} H_2 (385 μmol h^{-1} g^{-1}), while replacing water with a water–methanol mixture (without Na_2S/Na_2SO_3) further increased the H_2 yield to 1440 μmol g^{-1} (480 μmol h^{-1} g^{-1}). Finally, panel d illustrates the correlation between H_2 output and Cu loading, highlighting a monotonic increase in both sacrificial agent-free and sacrificial agent-assisted rates across the 0–20% Cu range. Fig. S6 shows the XRD patterns of the best-performing sample, 20% Cu-ZAO, before and after 180 min of irradiation, together with the corresponding ICSD reference pattern (no. 121152). The patterns confirm that the sample retains its spinel structure after irradiation, with no detectable formation of impurity phases.

Table 6 H_2 production rates with and without a sacrificial agent

	Without sacrificial agent		With sacrificial agent	
Sample	H_2 produced in 3 h (μmol g^{-1})	Avg. H_2 produced (μmol h^{-1} g^{-1})	H_2 produced in 3 h (μmol g^{-1})	Avg. H_2 produced (μmol h^{-1} g^{-1})
ZAO Air	72	24.0	291	97.0
1% Cu-ZAO	118	39.3	456	152
2% Cu-ZAO	138	46.0	639	213
5% Cu-ZAO	140	46.7	779	260
10% Cu-ZAO	190	63.3	962	321
20% Cu-ZAO	288	96.0	1155	385

To contextualise our results with respect to benchmark aluminate spinels reported in the literature, average H_2 evolution rates (μmol h^{-1} g^{-1}) with and without sacrificial reagents were compiled and are shown in Fig. 14. In the absence of any sacrificial agent (panel a), literature-reported $MgAl_2O_4$, $SrAl_2O_4$ and $BaAl_2O_4$ exhibit low activities, producing only 5.5, 6 and 1.5 μmol h^{-1} g^{-1}, respectively.[49] $ZnAl_2O_4$, $Zn_{0.9}Cu_{0.1}Al_2O_4$ and $Zn_{0.5}Cu_{0.5}Al_2O_4$ deliver improved yields of 47.3, 25.7, and 31.1 μmol h^{-1} g^{-1}, respectively.[50] In comparison with these aluminate spinels, the present work achieves 24.0 μmol h^{-1} g^{-1} for undoped ZAO-Air, while Cu incorporation at 1 to 20% progressively enhanced the rates from 39.3 to 96.0 μmol h^{-1}

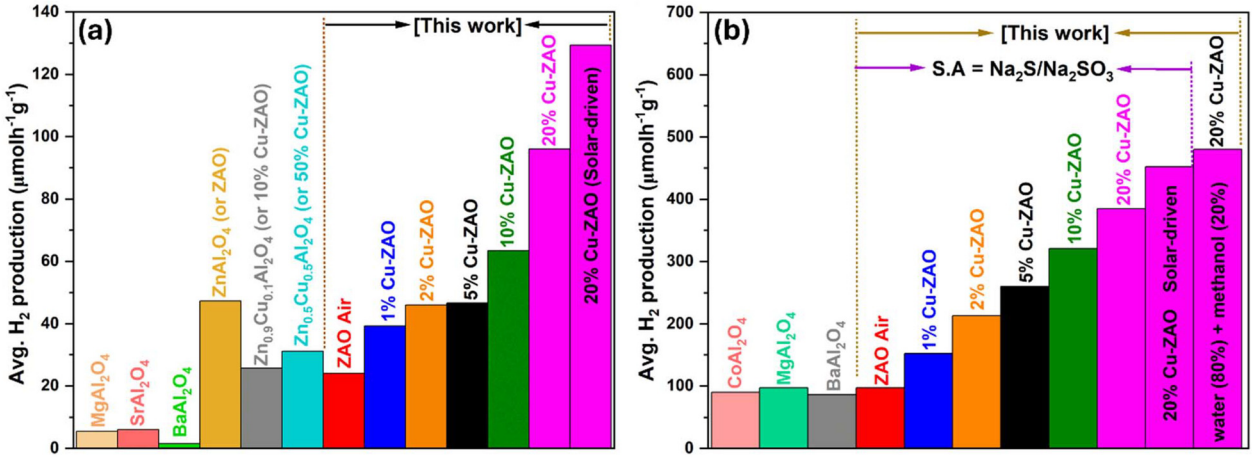

Fig. 14 Comparison of H_2 production performance with literature reports for phase-pure aluminates: (a) without a sacrificial agent and (b) with a sacrificial agent.

g^{-1}, respectively. Notably, solar-driven H_2 evolution for 20% Cu-ZAO reached 129.3 μmol h^{-1} g^{-1}.

Data for photocatalytic hydrogen production in the presence of a sacrificial agent are compared in Fig. 14(b). $CoAl_2O_4$ (S.A: glycerol) gave a yield of 90 μmol h^{-1} g^{-1},[51] while $MgAl_2O_4$ and $BaAl_2O_4$ (S.A.: triethanolamine) achieved yields of 97 and 86 μmol h^{-1} g^{-1}, respectively.[52] In comparison, with Na_2S/Na_2SO_3 as the sacrificial agent, ZAO-Air in the present work achieved 97 μmol h^{-1} g^{-1}. The Cu-ZAO series showed a substantial increase in activity, from 152 μmol h^{-1} g^{-1} at 1% Cu-doping to 320.7 μmol h^{-1} g^{-1} at 10%, and 452 μmol h^{-1} g^{-1} at 20%, culminating in 480 μmol h^{-1} g^{-1} in the water–methanol trial. These comparisons underscore the exceptional activity of these Cu-doped $ZnAl_2O_4$ spinels, particularly under visible–light conditions and with sacrificial agents, positioning our 20% Cu-ZAO photocatalyst among the highest-performing phase-pure spinel aluminates reported to date.

4. Conclusions

This study demonstrates the successful development of high-performance, dual-functional mesoporous $Zn_{1-x}Cu_xAl_2O_4$ (x = 0.01–0.20) spinel photocatalysts *via* a modified sol–gel citrate route. Calcination under nitrogen with a restricted oxygen supply effectively utilized residual citrate-derived carbon to constrain crystal growth, yielding phase-pure nanocrystalline materials with dramatically enhanced textural properties. Key structural and functional outcomes are:

1. Superior morphology and textural properties. Calcination under limited oxygen conditions resulted in a fourfold increase in specific surface area (up to 88.77 m^2 g^{-1}) compared with conventionally synthesized $ZnAl_2O_4$ (22.55 m^2 g^{-1}), together with high pore volume, uniform mesopores (5–8 nm) and significantly reduced crystallite sizes (15–20 nm *vs.* 36 nm). This porous, nanocrystalline architecture is ideal for catalytic applications requiring high accessibility to active sites and efficient mass transport.

2. Controlled Cu incorporation and defect engineering. Elemental mapping (EDS) confirmed homogeneous Cu incorporation within the spinel framework, while ICP-MS confirmed that the target stoichiometry of the $Zn_{1-x}Cu_xAl_2O_4$ materials was achieved. XPS analysis, together with lattice parameter deviations (XRD) provided strong evidence for an increasing oxygen vacancy concentration with increasing Cu doping.

3. Bandgap engineering and enhanced light harvesting. Progressive Cu doping induced significant bandgap narrowing from 3.95 eV (ZAO-Air) to 2.33 eV (20% Cu-ZAO), enabling extensive visible-light absorption (>400 nm), a critical advantage for solar-driven applications.

4. Optimized charge carrier dynamics. Photoluminescence (PL) quenching and dramatically extended intensity-weighted exciton lifetimes (>19 ns for Cu-doped samples *vs.* 3.15 ns for undoped ZAO), as revealed by time-resolved PL, confirmed the role of deep-trap states (identified primarily as oxygen vacancies) in suppressing detrimental radiative recombination and promoting long-lived charge separation, essential for photocatalysis.

5. Exceptional photocatalytic performance:

• Dye degradation. The Cu-doped catalysts exhibited dramatically enhanced photocatalytic degradation of Congo Red under UV-visible light. The 10% Cu-ZAO composition delivered the highest activity, significantly outperforming ZAO-Air.

• Hydrogen evolution. Optimized Cu doping, particularly in the 20% Cu-ZAO catalyst, achieved record hydrogen evolution rates among phase-pure aluminate spinels. Under pure visible light (>400 nm) with Na_2S/Na_2SO_3 as sacrificial agents, it produced 385 μmol h^{-1} g^{-1} H_2. Remarkably, it also demonstrated high practicality under challenging sacrificial-agent-free conditions, yielding 96 μmol h^{-1} g^{-1} H_2 under visible light alone. Performance was further boosted to 480 μmol h^{-1} g^{-1} using a water–methanol mixture under visible light.

This work establishes a robust and tunable platform for designing efficient dual-functional photocatalysts. The synergistic combination of high surface area, tailored mesoporosity, controlled Cu doping, oxygen vacancy generation, bandgap narrowing, and enhanced charge carrier dynamics underpins the exceptional activity observed in both environmental remediation (dye degradation) and sustainable energy production (H_2 evolution). Crucially, the high performance of the 20% Cu-ZAO photocatalyst under pure visible light, both with and without sacrificial agents, highlights its practical potential for solar-driven applications. Future work will focus on developing heterostructures using the same *in situ* carbon templating method, coupling these optimized spinels with other compatible semiconductors to construct Z-scheme or type-II junctions. These architectures could further suppress carrier recombination, expand spectral response, and enhance charge separation efficiency and potentially boost photocatalytic performance beyond current limits for both environmental and energy applications.

Author contributions

Syed Ansar Ali Shah: conceptualization, methodology, investigation, writing – original draft, writing – review & editing. Mudasar Nazir: investigation, writing – review & editing. Steve Dunn: resources, writing – review & editing. Muhammad Tariq Sajjad: supervision, conceptualization, funding acquisition, resources, writing – review & editing. Richard Baker: supervision, conceptualization, resources, writing – review & editing, funding acquisition, project administration.

Conflicts of interest

There are no conflicts to declare.

Data availability

Key data underpinning this article are available on the PURE repository of the University of St Andrews at https://research-portal.st-andrews.ac.uk/en/persons/richard-baker/datasets/ and

at DOI https://doi.org/10.17630/240ea6c3-943e-419f-9f88-c1385f70f8dc.

Supplementary information (SI): EDS maps of intermediate product; chemical composition comparison by EDS, XPS and ICPMS; band edge potential information; UV-Visible spectra obtained during the Congo Red degradation experiments; reusability test results for dye degradation tests; and XRD patterns for 20%Cu-ZAO before and after use in H_2 generation experiments. See DOI: https://doi.org/10.1039/d6nr00820h.

Acknowledgements

We gratefully acknowledge financial support for the PhD scholarship of SAAS, jointly funded by the Higher Education Commission (HEC) of Pakistan, the University of St Andrews, and London South Bank University (LSBU). MN acknowledges funding from LSBU for his PhD. XPS was carried out at the XPS facility of the University of St Andrews by Dr F. Grillo. S/TEM and EDS analyses were performed at the Electron Microscopy Facility, University of St Andrews, by Dr A. Naden. We acknowledge support for the centre from the Engineering and Physical Sciences Research Council of the UK (EP/L017008/1, EP/R023751/1, EP/T019298/1 and UKRI647). ICP-MS analysis was performed at the University of Edinburgh.

References

1 C. Bie, H. Yu, B. Cheng, W. Ho, J. Fan and J. Yu, *Adv. Mater.*, 2021, **33**, 2003521.
2 D. Gunawan, J. Zhang, Q. Li, C. Y. Toe, J. Scott, M. Antonietti, J. Guo and R. Amal, *Adv. Mater.*, 2024, **36**, 2404618.
3 S. Chen, T. Takata and K. Domen, *Nat. Rev. Mater.*, 2017, **2**, 17050.
4 A. Fujishima and K. Honda, *Nature*, 1972, **238**, 37–38.
5 J. Ran, J. Zhang, J. Yu, M. Jaroniec and S. Z. Qiao, *Chem. Soc. Rev.*, 2014, **43**, 7787–7812.
6 T. Takata, J. Jiang, Y. Sakata, M. Nakabayashi, N. Shibata, V. Nandal, K. Seki, T. Hisatomi and K. Domen, *Nature*, 2020, **581**, 411–414.
7 H. Fu, Y. Wu, Y. Guo, T. Sakurai, Q. Zhang, Y. Liu, Z. Zheng, H. Cheng, Z. Wang, B. Huang, Q. Wang, K. Domen and P. Wang, *Nat. Commun.*, 2025, **16**, 990.
8 T. K. Saothayanun, Y. Inchongkol, N. Weeranoppanant, M. Kondo, M. Ogawa and S. Bureekaew, *J. Mater. Chem. A*, 2024, **12**, 26743–26748.
9 H. Li, S. Wang, H. Chi and C. Li, *ChemPhotoChem*, 2024, **8**, e202300049.
10 L. Ran, J. Hou, S. Cao, Z. Li, Y. Zhang, Y. Wu, B. Zhang, P. Zhai and L. Sun, *Sol. RRL*, 2020, **4**, 1900487.
11 M. D. Ashie and B. P. Bastakoti, *Small*, 2024, **20**, 2310927.
12 Y. Zhou, J. Liu, R. Pi, Q. Liu, R. Liu and J. Yang, *Int. J. Hydrogen Energy*, 2024, **85**, 683–693.
13 S. R. Damkale, S. S. Arbuj, G. G. Umarji, S. B. Rane and B. B. Kale, *RSC Adv.*, 2021, **11**, 7587–7599.
14 Y. Huang, Y. Yu, Y. Yu and B. Zhang, *Sol. RRL*, 2020, **4**, 2000037.
15 S. A. A. Shah, N. Gkoulemani, J. T. S. Irvine, M. T. Sajjad and R. Baker, *J. Catal.*, 2024, **439**, 115769.
16 F. Sakina, J. M. Muñoz-Ocaña, A. Bouziane, M. Lopez-Haro and R. T. Baker, *Nanoscale Adv.*, 2019, **1**, 4772–4782.
17 A. Talati and M. Haghighi, *J. Photochem. Photobiol., A*, 2022, **430**, 113955.
18 D. H. Murthy, V. Nandal, A. Furube, K. Seki, R. Katoh, H. Lyu, T. Hisatomi, K. Domen and H. Matsuzaki, *Adv. Energy Mater.*, 2023, **13**, 2302064.
19 J. Liu, J. Wan, L. Liu, W. Yang, J. Low, X. Gao and F. Fu, *Chem. Eng. J.*, 2022, **430**, 133125.
20 F. F. Alharbi, S. Aman, M. Abdullah, A. G. Abid, S. Manzoor, R. Y. Khosa, H. M. T. Farid, M. V. Silibin, S. V. Trukhanov, T. I. Zubar and A. V. Trukhanov, *Ceram. Int.*, 2024, **50**, 24177–24185.
21 T. Tangcharoen, J. T-Thienprasert and C. Kongmark, *Int. J. Appl. Ceram. Technol.*, 2021, **18**, 1125–1143.
22 K. K. Kumar, T. S. Kumar, B. R. Reddy, C. S. Chakra, K. Praveena and S. Katlakunta, *J. Sol-Gel Sci. Technol.*, 2024, **111**, 794–805.
23 T. R. Gurugubelli, B. Babu and K. Yoo, *Energies*, 2021, **14**, 2869.
24 S. Yuvaraj, S. Revathi, A. Kumar, G. Anitha, A. M. Al-Enizi, B. Pandit, R. Revathi, M. Sundararajan, C. Prakash, R. S. R. Isaac, H. Payal, N. Tarannum and M. Ubaidullah, *Opt. Mater.*, 2023, **145**, 114423.
25 S. A. A. Shah, A. Sultan, K. Zheng, M. T. Sajjad and R. Baker, *J. Mater. Chem. A*, 2025, **13**, 29486–29503.
26 T. Tangcharoen, W. Klysubun, T. Jiraroj and C. Kongmark, *J. Solid State Chem.*, 2020, **292**, 121695.
27 T. M. Modungwe, G. L. Kabongo, P. S. Mbule, K. Makgopa, E. Coetsee and M. S. Dhlamini, *Sci. Rep.*, 2024, **14**, 25837.
28 H. P. Klug and L. E. Alexander, *X-ray diffraction procedures: for polycrystalline and amorphous materials*, Wiley, New York, 1974, p. 992.
29 Y. Jamil, G. P. Jeyakumar and G. Deivasigamani, *Mater. Process.*, 2023, **14**, 2.
30 M. Tyunina, O. Pacherova, T. Kocourek and A. Dejneka, *Sci. Rep.*, 2021, **11**, 15247.
31 J. H. Weng, M. C. Kao, K. H. Chen and M. Z. Li, *Nanomaterials*, 2023, **13**, 2685.
32 V. S. Kirankumar and S. Sumathi, *Mater. Res. Bull.*, 2017, **93**, 74–82.
33 Y. Behnamian, E. Aghaie, D. Serate, Z. Tolentino, H. Niazi and A. Mostafaei, *Ceram. Int.*, 2022, **48**, 27988–27994.
34 T. Tangcharoen, J. T-Thienprasert and C. Kongmark, *J. Mater. Sci.: Mater. Electron.*, 2018, **29**, 8995–9006.
35 A. V. Belyaev, M. I. Lelet, N. I. Kirillova, N. M. Khamaletdinova, M. S. Boldin, A. A. Murashov and S. S. Balabanov, *Ceram. Int.*, 2019, **45**, 4835–4839.
36 M. Thommes, K. Kaneko, A. V. Neimark, J. P. Olivier, F. Rodriguez-Reinoso, J. Rouquerol and K. S. W. Sing, *Pure Appl. Chem.*, 2015, **87**, 1051–1069.
37 F. M. Chang, S. Brahma, J. H. Huang, Z. Z. Wu and K. Y. Lo, *Sci. Rep.*, 2019, **9**, 905.

38 M. Hu, H. Hu, S. Tang and Z. Pan, *Catalysts*, 2022, **12**, 1511.
39 Y. Liu, H. Zhang, W. Fu, Z. Yang and Z. Li, *J. Mater. Sci.: Mater. Electron.*, 2018, **29**, 18797–18806.
40 R. Tan, S. W. Hwang, A. Sivanantham and I. S. Cho, *J. Catal.*, 2021, **400**, 218–227.
41 L. Shi, P. Yan, Z. Gao and W. Huang, *Arabian J. Chem.*, 2023, **16**, 104464.
42 R. Mane, A. Potdar, Y. Jeon and C. Rode, *Top. Catal.*, 2025, **68**, 318–331.
43 F. Z. Akika, M. Benamira, H. Lahmar, M. Trari, I. Avramova and Ş. Suzer, *Surf. Interfaces*, 2020, **18**, 100406.
44 A. Le Nestour, M. Gaudon, G. Villeneuve, M. Daturi, R. Andriessen and A. Demourgues, *Inorg. Chem.*, 2007, **46**, 4067–4078.
45 K. Hu, S. Zhang, Z. Mao, D. Zhao, D. Li, Z. Li, Q. Li, Q. Tang and T. Shi, *RSC Adv.*, 2025, **15**, 14739–14744.
46 S. Baruah, B. Maibam, J. Jaiswal, A. Kumar and S. Kumar, *Sens. Diagn.*, 2023, **2**, 1236–1248.
47 P. Makuła, M. Pacia and W. Macyk, *J. Phys. Chem. Lett.*, 2018, **9**, 6814–6817.
48 N. Pathak, P. S. Ghosh, S. Saxena, D. Dutta, A. K. Yadav, D. Bhattacharyya, S. N. Jha and R. M. Kadam, *Inorg. Chem.*, 2018, **57**, 3963–3982.
49 C. Gómez-Solís, S. L. Peralta-Arriaga, L. M. Torres-Martínez, I. Juárez-Ramírez and L. A. Díaz-Torres, *Fuel*, 2017, **188**, 197–204.
50 S. J. Castañeda-Palafox, L. A. Diaz-Torres, L. E. Puentes-Prado and C. Gómez-Solís, *Int. J. Hydrogen Energy*, 2024, **51**, 1279–1291.
51 A. Basaleh and M. H. H. Mahmoud, *ACS Omega*, 2021, **6**, 10428–10436.
52 T. J. Mumanga, L. A. Diaz-Torres, E. Montes and C. Gómez-Solís, *Appl. Opt.*, 2020, **59**, D246–D252.